Journal of Metamorphic Geology

WILEY

Journal of METAMORPHIC GEOLOGY

ORIGINAL ARTICLE OPEN ACCESS

An Inverse Method for Quantifying Petrological Parameters and Uncertainty in Phase Equilibrium Modelling

T. Mackay-Champion[1] | I. P. Cawood[1,2]

[1]Department of Earth Sciences, University of Oxford, Oxford, UK | [2]Department of Earth and Planetary Sciences, The University of Hong Kong, Hong Kong

Correspondence: I. P. Cawood (ipcawood@hku.hk)

Received: 20 August 2024 | **Revised:** 28 September 2025 | **Accepted:** 2 October 2025

Funding: This work is supported by the Oxford-Radcliffe Graduate Scholarship, BHP, Natural Environment Research Council (NE/L002612/1) and the Hong Kong RGC (JLFS/P-702/24 and 17308023).

ABSTRACT

Phase equilibrium modelling offers a powerful quantitative framework for understanding petrological processes. Yet, many studies still rely on qualitative comparisons between natural datasets and these forward modelled predictions to constrain model parameters, commonly pressure–temperature (*P–T*) conditions. Compounding this, uncertainties from the observed data or within the modelled predictions are rarely quantified, limiting confidence in the estimated *P–T* conditions and resulting petrological interpretations. We introduce LinaForma, an inverse modelling workflow that determines best-fit *P–T* conditions (or other petrological parameters) and their associated uncertainties for a given rock system by minimizing the misfit between observed data (e.g., mineral compositions or modal proportions) and their forward modelled predictions. Uncertainty is quantified by resampling of the observed data with replacement. Diagnostic metrics identify poorly performing variables and assess the sensitivity of the inversion result to variable uncertainty. Applied to an amphibolite-facies pelite and metabasite from the Greater Himalayan Sequence (Zanskar Himalaya, NW India), the approach proves effective across contrasting model systems that require different sets of solution models and variables, and it produces *P–T* estimates consistent with classical thermobarometry. The workflow offers several advantages: compatibility with outputs from any forward modelling software; flexible variable selection; systematic grid-search inversion in multidimensional space; a robust L1-norm misfit function resistant to outliers; and sensitivity and uncertainty analysis via bootstrap resampling. Limitations include the increasing computational demands for high-dimensional grids ($N > 2$) and the absence of explicit quantification of uncertainties inherited from the thermodynamic dataset and solution models. Alongside other emerging quantitative methods, LinaForma enables petrologists to make more informed interpretations of complex metamorphic systems and target improvements to thermodynamic datasets.

1 | Introduction

Phase equilibrium modelling is integral to modern metamorphic petrology, providing a powerful quantitative framework to decipher the evolution of metamorphic sequences and, in turn, offering critical insights into the processes that shape Earth's crust and mantle. This modelling is built on large datasets including thermodynamic end-member properties and activity–composition (*a–X*) relations of minerals, fluid and melt (e.g., Berman 1988; Holland and Powell 1998). When integrated with appropriate software, these datasets can be used to produce sophisticated forward models that predict equilibrium phase assemblages, compositions and modal proportions, alongside numerous other variables across pressure–temperature–composition (*P–T–X*) space (e.g., Spear et al. 2016).

Despite the quantitative foundation of these techniques, petrological studies predominantly reconstruct the metamorphic

T.Mackay-Chamion and I.P. Cawood are co-first authors.

evolution of a rock using qualitative to semi-quantitative comparisons between the measured values from the rock and their forward modelled predictions (Powell and Holland 2008). The quality of these comparisons depends on understanding the uncertainties associated with both the input data and the modelling process. As is standard in most scientific fields, any calculation must include a quantifiable estimate of uncertainties, alongside recognition of uncertainties that cannot be readily quantified (Powell and Holland 1994, 2008). However, in petrological studies, such uncertainties are often overlooked, such that derived model parameters, commonly *P–T* conditions, cannot be interpreted within a defined confidence range, thereby limiting confidence in the resulting petrological interpretations.

Although several programs employ quantitative approaches for determining optimal *P–T* conditions (e.g., Berman 1991; Gordon 1992; Powell and Holland 1994; Duesterhoeft and Lanari 2020; Nerone et al. 2025), many of these tools are tied to specific software, are not integrated with phase equilibrium modelling, or do not place a strong emphasis on uncertainty quantification. Therefore, the impact of uncertainties on *P–T* estimates produced by current thermobarometric techniques remains difficult to assess. To address these limitations, we present LinaForma, a flexible workflow that quantitatively determines the best-fit *P–T* solution and associated uncertainty for a given rock system. In this study, we (1) outline the method and provide guidelines for using the workflow, (2) apply it to a pelite (or metapelite) and metabasite sample to test its effectiveness across contrasting metamorphic systems, (3) compare it with other quantitative approaches and (4) highlight the advantages, potential limitations, and avenues for future work for quantitative methods.

2 | Inversion Method

Forward modelling is the process of predicting the data one would observe for a given set of model input parameters. A pseudosection is an example of a forward model, in which the equilibrium phase assemblage, phase compositions and proportions are predicted for a rock of a given chemical composition across *P–T* space. This is contrasted with inverse modelling in which observed data is used to estimate the underlying model parameters. Single-equilibrium thermobarometry (e.g., Ti-in-biotite geothermometer; Henry et al. 2005) and multi-equilibrium thermobarometry (Powell and Holland 1994) are examples of inverse methods, where *P–T* conditions are estimated from the observed mineral compositions.

Constraining the conditions of equilibration and evolution of a rock is frequently undertaken using intersecting isopleths of observed phase compositions or modal proportions calculated using phase equilibrium modelling. In its simplest form, a mean or representative analysis from two variables can be used to determine a singular crossover point in *P–T* space (Figure 1a). When comparing the data distribution of two or more variables, the situation becomes more complex, especially when the variables have markedly different observed data distributions or sensitivities to *P–T*, such that even a narrow observed population distribution can correspond to a broad calculated *P–T* interval if the variable is highly sensitive to *P–T* changes (Figure 1b). Additional variables may make for a more 'representative' result but can also result in multiple zones of overlap (Figure 1c) or poor to no agreement (Figure 1d). Although this method has been effectively applied to semi-quantitatively analyse the tectonothermal evolution of metamorphic terranes (e.g., Vance and Mahar 1998; Hoschek 2004; Štípská and Powell 2005), the accuracy and precision of the resulting *P–T* estimates, and thereby the conclusions drawn from the sample, are significantly influenced by the variables selected and their associated uncertainties (Figure 1a–d).

To address these challenges, the workflow presented in this study, LinaForma, inverts a large set of variables simultaneously and uses the uncertainties in the mineral measurements to estimate variability in the derived *P–T* estimates (Figure 1e). For clarity, we present the method for *P–T* conditions, though it is equally applicable to any set of model parameters of interest. The workflow uses a grid-search inversion, which minimizes misfit between the mineral measurements and their forward modelled predictions (Figure 2a), coupled with bootstrap resampling of mineral measurements (Figure 2b), to quantify the best-fit *P–T* conditions and associated uncertainties for a given bulk rock composition. We focus specifically on uncertainties in the mineral measurements because they reflect the scale of equilibrium preserved in natural samples, constrain the precision of the results and can be readily incorporated into uncertainty analysis. Uncertainties in the thermodynamic end-member dataset and in the interaction energies used in the activity-composition (a–X) relationships also contribute significantly to the overall *P–T* uncertainty (Powell and Holland 1988, 2008). However, properly accounting for these effects requires recalculating the forward model for each variation—a computationally intensive process—and the uncertainties are not always well constrained. Although these uncertainties are not explicitly estimated in this workflow; the bootstrap resampling approach inherently reflects some of the additional dispersion they introduce. As a large number of mineral composition variables are used in this study, their definitions are included in Table 1 for reference.

2.1 | Best-Fit *P–T* Conditions: The Grid-Search Inversion

A grid-search inversion is used to determine the optimal or best-fit *P–T* conditions for a given rock system. The grid-search involves drawing a large number of trial solutions from a regular grid in model (e.g., *P–T*) space. For each point on the grid (i.e., a trial solution), the difference between the forward model's predicted data and the observed data is computed using an objective, or misfit, function (Figure 2a). The best-fit solution is the point on the grid with the lowest value of the misfit function. In this case, the observed data may include mineral compositions, mineral modal proportions, and bulk properties such as the interpreted equilibrium phase assemblage and whole-rock density. The forward models for each point on the grid can be calculated using programs such as Theriak-Domino (de Capitani and Brown 1987; de Capitani and Petrakakis 2010), Perple_X (Connolly 1990, 2005) and MAGEMin (Riel et al. 2022).

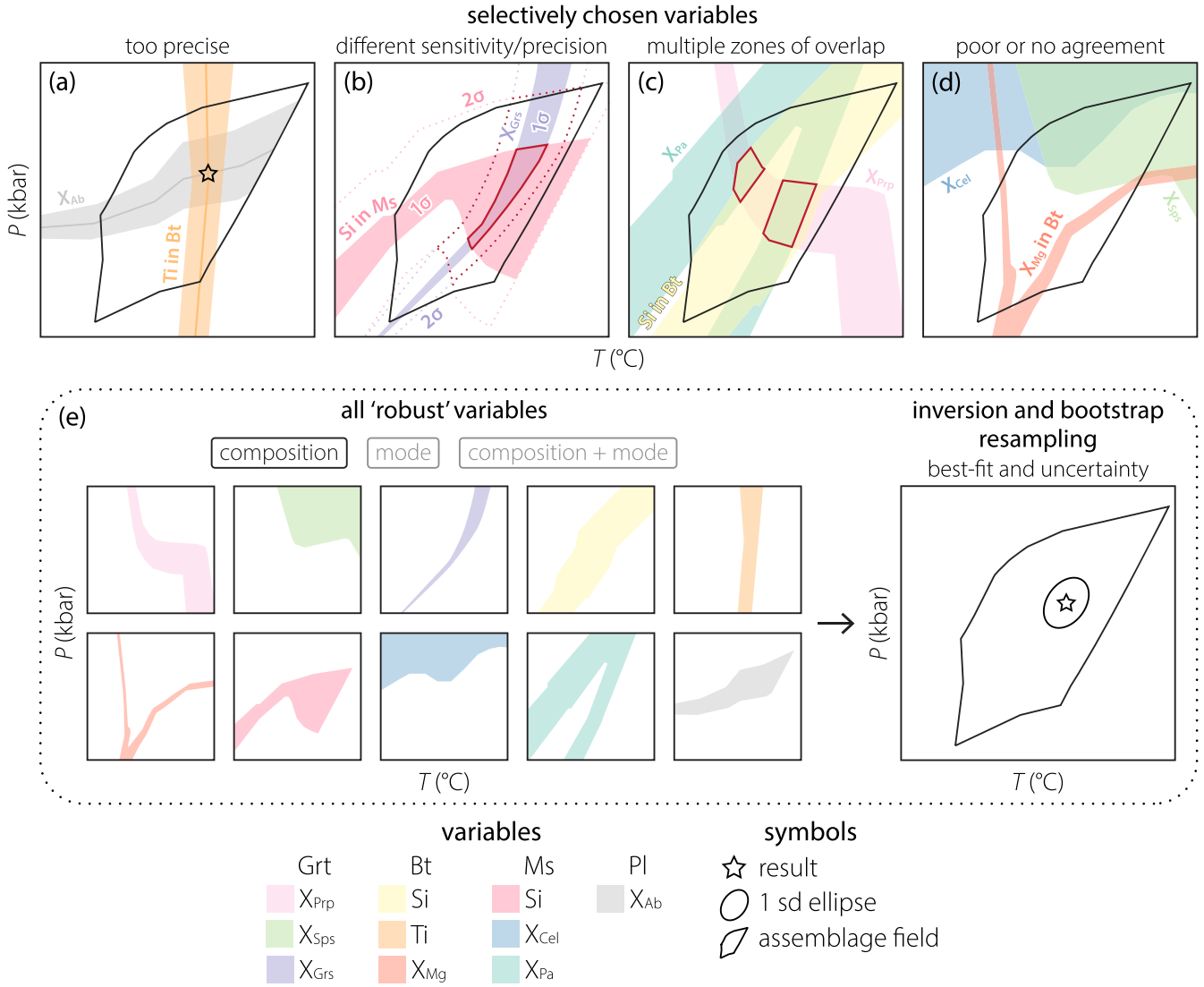

FIGURE 1 | Schematic summary of (a–d) common problems associated with application of intersecting mineral composition variables commonly applied in constraining the *P–T* conditions from forward models. (e) Using a large and diverse range of robust mineral measurement variables (composition, modal proportion or both) to provide a more representative *P–T* constraint using grid-search inversion and bootstrap resampling. Definitions of mineral composition variables are included in Table 1 for reference.

This workflow employs a normalized L1-type misfit function (**Φ**), expressed as the sum of absolute residuals scaled by the observed values (Equation 1):

$$\Phi = \sum_{i=1}^{N} \frac{|\, x_i^{\text{obs}} - x_i^{\text{mod}} \,|}{x_i^{\text{obs}}} \tag{1}$$

where N is the total number of variables, x_i^{mod} is the modelled value of variable i predicted at the trial solution and x_i^{obs} is the observed value of variable i. The residuals are scaled relative to the observed value of each variable to ensure that variables with large magnitudes do not have an overwhelming influence on the result. Large values of Φ suggest the model predictions poorly fit the observed data, whereas low values of Φ show the observed data and the model predictions are similar (i.e., the data 'residuals' are small). The trial solution with the lowest value of Φ is the best-fit solution.

2.2 | Uncertainty Analysis: Bootstrap Resampling

Bootstrap resampling is used to estimate the uncertainty associated with the best-fit *P–T* solution. This involves resampling the observational data with replacement and then computing the required statistics for each resampled dataset, in this case the best-fit solution of the grid-search inversion (Figure 2b). When repeated multiple times (e.g., $N \geq 1000$), the distribution of inversion solutions obtained from the resampled datasets provides an estimate of the true mean or median solution and the population distribution (Menke 1984).

Bootstrap resampling can be either non-parametric or parametric. Non-parametric bootstrapping involves resampling with replacement from the original observational dataset. Parametric bootstrapping generates samples according to an assumed distribution of the observational data (Efron 1979), in this case a normal distribution (Figure 2b). Given that the

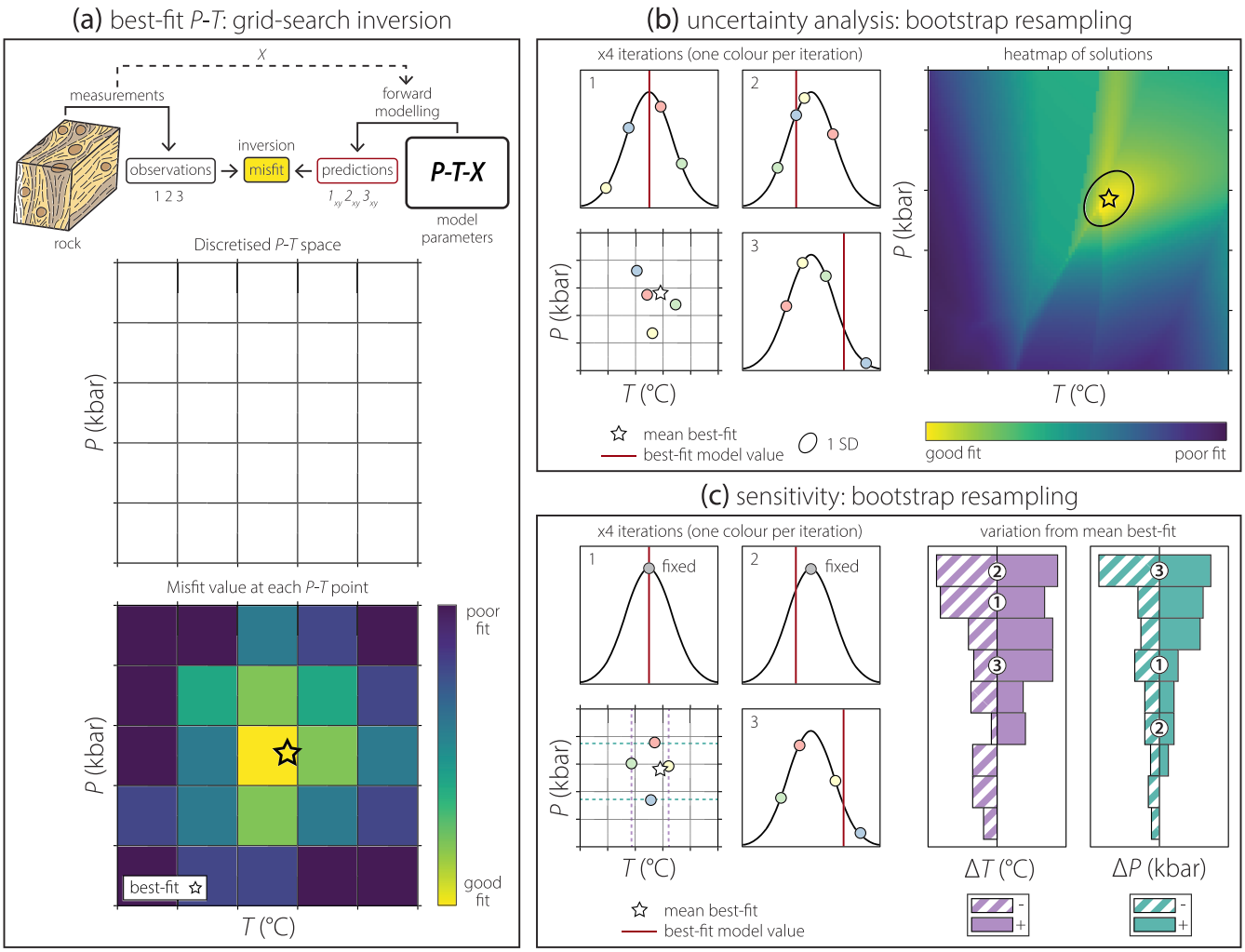

FIGURE 2 | Schematic summary of the new workflow. From (a) grid-search non-linear inversion to determine the best-fit *P–T* conditions of a given rock system, to (b) bootstrap resampling to assess the uncertainty of the *P–T* solution and (c) solution assessment using bootstrap resampling of the employed variables to estimate sensitivity of the best-fit result to uncertainty in the individual variables. Variables 1, 2, and 3 are randomly sampled from their distributions, with colour representing trial number or iteration. Thin-section schematic from Palin et al. (2016).

probability density function in non-linear problems is typically non-Gaussian (Menke 1984), percentile-based confidence intervals such as the interquartile range (IQR) are often more informative than the standard deviation and are therefore preferred for results where possible. Bootstrap-resampling is also used to assess the sensitivity of the inversion results to uncertainty in each variable (Section 2.3.3 and Figure 2c).

2.3 | Diagnostics

The workflow includes three diagnostics with which to validate and refine the best-fit solution: (1) quality of data fit (f_i, f_{total}) between the best-fit solution and the observations, (2) the influence of each variable ($f_{\text{total}(i)}$) on the best-fit solution and (3) the sensitivity of the best-fit solution (ΔP_i, ΔT_i) to uncertainty in each of the chosen variables. The values of these diagnostic metrics and full results for each solution are automatically output in table format at the end of the inversion calculations. The definitions for each value reported in the results table are included in Table 2.

2.3.1 | Quality of Data Fit (f_i, f_{total})

The data fit metric assesses the level of agreement between the observations and the median best-fit solution (after bootstrap resampling). This is quantified by assessing whether the model's predictions at the median best-fit conditions (e.g., the modelled value of X_{Alm} garnet at PT_{best}) fall within two standard deviations of the observed values. This assessment is provided in the workflow by a score for each variable (f_i) and a total score (f_{total}). These are calculated following Equations (2) and (3), respectively:

$$f_i = \frac{|\, x_i^{\text{obs}} - x_i^{\text{mod}} \,|}{2\sigma_i^{\text{obs}}} \tag{2}$$

$$f_{\text{total}} = \frac{1}{N} \sum_{i=1}^{N} f_i \tag{3}$$

where N is equal to the total number of variables, x_i^{mod} represents the modelled value of variable i predicted at the best-fit solution, x_i^{obs} represents the observed value of variable i and

TABLE 1 | Mineral composition variable definitions for common pelitic and metabasic minerals at sub-solidus conditions. *N.b.* Maintain one degree of freedom where appropriate.

Mineral	Variable	Definition
Grt	X_{Alm}	$\frac{\mathrm{Fe^{2+}}}{\mathrm{Fe^{2+}+Mg+Ca+Mn}}$
	X_{Grs}	$\frac{\mathrm{Ca}}{\mathrm{Fe^{2+}+Mg+Ca+Mn}}$
	X_{Sps}	$\frac{\mathrm{Mn}}{\mathrm{Fe^{2+}+Mg+Ca+Mn}}$
	X_{Prp}	$\frac{\mathrm{Mg}}{\mathrm{Fe^{2+}+Mg+Ca+Mn}}$
	X_{Mg}	$\frac{\mathrm{Mg}}{\mathrm{Mg+Fe^{2+}}}$
Grt (−Mn)	X_{Alm}	$\frac{\mathrm{Fe^{2+}}}{\mathrm{Fe^{2+}+Mg+Ca}}$
	X_{Grs}	$\frac{\mathrm{Ca}}{\mathrm{Fe^{2+}+Mg+Ca}}$
	X_{Prp}	$\frac{\mathrm{Mg}}{\mathrm{Fe^{2+}+Mg+Ca}}$
	X_{Mg}	$\frac{\mathrm{Mg}}{\mathrm{Mg+Fe^{2+}}}$
St	X_{Mg}	$\frac{\mathrm{Mg}}{\mathrm{Mg+Fe^{2+}}}$
Crd	X_{Mg}	$\frac{\mathrm{Mg}}{\mathrm{Mg+Fe^{2+}}}$
Chl	X_{Mg}	$\frac{\mathrm{Mg}}{\mathrm{Mg+Fe^{2+}}}$
Bt	Si	apfu
	Ti	apfu
	X_{Mg}	$\frac{\mathrm{Mg}}{\mathrm{Mg+Fe^{2+}}}$
Ms	Si	apfu
	X_{Cel}	Mg apfu
	X_{Pa}	$\frac{\mathrm{Na}}{\mathrm{Na+Ca+K}}$
Pl	X_{Ab}	$\frac{\mathrm{Na}}{\mathrm{Na+Ca+K}}$
	X_{An}	$\frac{\mathrm{Ca}}{\mathrm{Na+Ca+K}}$
Kfs	X_{San}	$\frac{\mathrm{K}}{\mathrm{Na+Ca+K}}$
Ep	X_{Fe}	$\frac{\mathrm{Fe^{3+}}}{\mathrm{Al+Fe^{3+}}}$
Amph	Ti	apfu
	Ts	Al(T) − Na(A) − K(A)
	Ed	Na(A) + K(A)
	Gln	Na(M4)
Cpx	Al	apfu
	X_{Mg}	$\frac{\mathrm{Mg}}{\mathrm{Mg+Fe^{2+}}}$
	Ca	apfu
	X_{Jd}	$\begin{cases}\mathrm{Na(M2)},\ \text{if Na(M2)} > \mathrm{Al(M1)}\\ \mathrm{Al(M1)},\ \text{if Al(M1)} > \mathrm{Na(M2)}\end{cases}$

σ_i^{obs} represents the observed standard deviation for variable i. A value of >1 for both the total score and the individual variable scores indicates a poor fit. A total score of ≤ 1 demonstrates that the inversion fits the data acceptably well, and an individual variable score of ≤ 1 indicates that the modelled prediction fits the observations within 2 standard deviations. The workflow provides options to visualize this relationship (e.g., Figure 3d). The scoring strategy above provides a similar function to the σ_{fit} metric (square root of the mean square weighted deviation) used in av*PT* (Powell and Holland 1994).

2.3.2 | Influence ($f_{\mathrm{total}(i)}$)

Influence analysis quantifies the impact of individual variables on the inversion result. Certain variables can exert strong leverage on the best-fit solution because of their behaviour or scaling of data range in model space. To identify whether a variable exerts disproportionate control, we compute a leave-one-out total fit, obtained by recalculating the best-fit solution after excluding variable i and using the mean values of all remaining variables. The corresponding is denoted as $f_{\mathrm{total}(i)}$. This metric demonstrates, for each variable, whether it disproportionately affects the solution and its exclusion improves overall inversion performance. The influence analysis provides a similar function to the dimensionless hat value (also called the leverage value) used to quantify the influence of individual end-members on the final result in av*PT* (Powell and Holland 1994).

2.3.3 | Sensitivity (ΔP_i, ΔT_i)

Whereas influence analysis quantifies the effect of removing a variable on the best-fit solution, sensitivity analysis estimates how uncertainty in the value of a variable affects the inversion result. This is performed using bootstrap resampling, in which each variable is resampled in turn and the remaining variables are fixed at the appropriate mean value (Figure 2c). The resultant spread in the best-fit solutions thus provides a measure of the inversion's sensitivity to the uncertainty in the resampled variable and the precision with which it constrains model space. The sensitivity values are given as the maximum absolute temperature (ΔT_i) and pressure (ΔP_i) difference between the mean solution of the inversion when all the variables are resampled (T^{mean}, P^{mean}) and the range of solutions when only a single variable, i, is resampled N times. These are shown in Equations (4) and (5):

$$T_i^{\mathrm{max\,/\,min}} = \overline{T}_i \pm 2\sigma_{T_i} \tag{4}$$

$$\Delta T_i = \max\left|\left(T^{\mathrm{mean}} - T_i^{\mathrm{min}}\right), \left(T_i^{\mathrm{max}} - T^{\mathrm{mean}}\right)\right| \tag{5}$$

where $\overline{T}_i$ represents the mean best-fit temperature from the resampling of variable i and σ_{T_i} represents the standard deviation temperature for variable i. The same equations apply for pressure.

The comparison is made with the mean solution rather than the median solution because the mean is less sensitive to the discretization of the model grid. A high sensitivity may be

TABLE 2 | Definitions of parameters used in the inversion analysis and values presented in the result output and diagnostics table.

Parameter	Definition
f_i	Quality of fit score for each variable. Higher values indicate a poorer fit
$f_{\text{total}(i)}$	Leave-one-out total fit for variable i; calculated by removing variable i, recalculating the best-fit solution and resulting total fit for remaining variables. Lower values indicate improved fit
ΔT_i	T sensitivity of best-fit solution to variable i; maximum absolute T variation from bootstrap resampling of variable i, with all other variables fixed. Measured relative to the mean best-fit solution of all variables
ΔP_i	P sensitivity of best-fit solution to variable i; maximum absolute P variation from bootstrap resampling of variable i, with all other variables fixed. Measured relative to the mean best-fit solution of all variables
$\mu_{\text{obs}} \pm 2\sigma$	Mean observed variable value, with two standard deviations (uncertainty)
Mod	Modelled value of variable for the median best-fit solution
Mean	Mean value of the temperature and pressure distribution
Median	Median value (50th percentile) of the temperature and pressure distribution
IQR	Interquartile range (25th–75th percentile) of the temperature and pressure distribution
f_{total}	Overall quality of fit score for the inversion; values above 1 indicate poor fit
Grid resolution	Resolution/spacing of the grid in°C and kbar
Bootstrap resamples	Number of bootstrap resamples

caused by a large spread in the value of observed data variables or a large percentage change in the model values over small areas of *P–T* space (meaning that small differences in input value results in a large change in pressure or temperature estimate). Sensitivity values are displayed using tornado plots (e.g., Figure 3e).

2.4 | Applying the Workflow

2.4.1 | Observations Setup

Any variable type can be used in the inversion, provided an appropriate forward model can be calculated, and the data can be tabulated into grid format. The type and choice of variables (e.g., mineral compositions and/or modal proportions) used should consider the interpreted scale of chemical and textural equilibrium, the method of bulk composition acquisition, the geological problem, model precision and the desired sensitivity of individual variables. Modal proportion variables may be used for major phases but should be used with caution for minor or accessory phases (Weller et al. 2024). Compositional variables can be expressed as full element concentrations (apfu) or as derived compositional variables (e.g., end-members, ratios and substitution vectors). Using apfu retains full compositional information and allows more direct uncertainty assessment, whereas derived compositional variables can reduce sensitivity to systematic model offsets where applied appropriately. Table 1 lists some recommended compositional variables for pelitic and metabasic lithologies in sub-solidus systems.

When selecting variables for inversion, maximise the number of constraints by including as many robust variables as possible from the widest range of phases interpreted to be in mutual equilibrium. At least one degree of freedom should be preserved for each set of non-independent variables. For example, for garnet, including three of either X_{Alm}, X_{Grs}, X_{Sps}, or X_{Prp} is sufficient, all four should not be used simultaneously. For each major phase within the model, including at least one variable will ensure that the misfit function accommodates its presence and for those with solid solution models, the major substitutions should be considered in the choice of variables. This ensures that the derived *P–T* uncertainty estimate reflects the largest proportion of the system. Zoned minerals such as garnet are a possible exception, as core compositions may be interrogated independently where appropriate. Note that the inferred equilibrium assemblage field is not inherently enforced as a constraint unless it is used explicitly as a variable or stable phases are assigned a non-zero mode (or vice versa). The advantages and limitations of this choice are discussed in Section 4.2.

If the bulk rock composition varies significantly across the analysed volume, the associated uncertainty can be quantified by computing a suite of forward models generated from Monte Carlo variations of the input composition used for forward modelling. The composition range may be defined from multiple analyses from different sample domains (e.g., Palin et al. 2016; Duesterhoeft and Lanari 2020) or a range characteristic of the observed scale of variation (e.g., 5%; Forshaw et al. 2019).

2.4.2 | Predictions Setup

The *P–T* grid should be broad enough to avoid boundary effects influencing the best-fit solutions while maintaining sufficient resolution to capture the true solution between grid points. The spacing should reflect the required precision of the problem, the precision of the input data, the model parameters and the model's sensitivity. If results converge on the boundary of the *P–T* range, a different range should be chosen if possible.

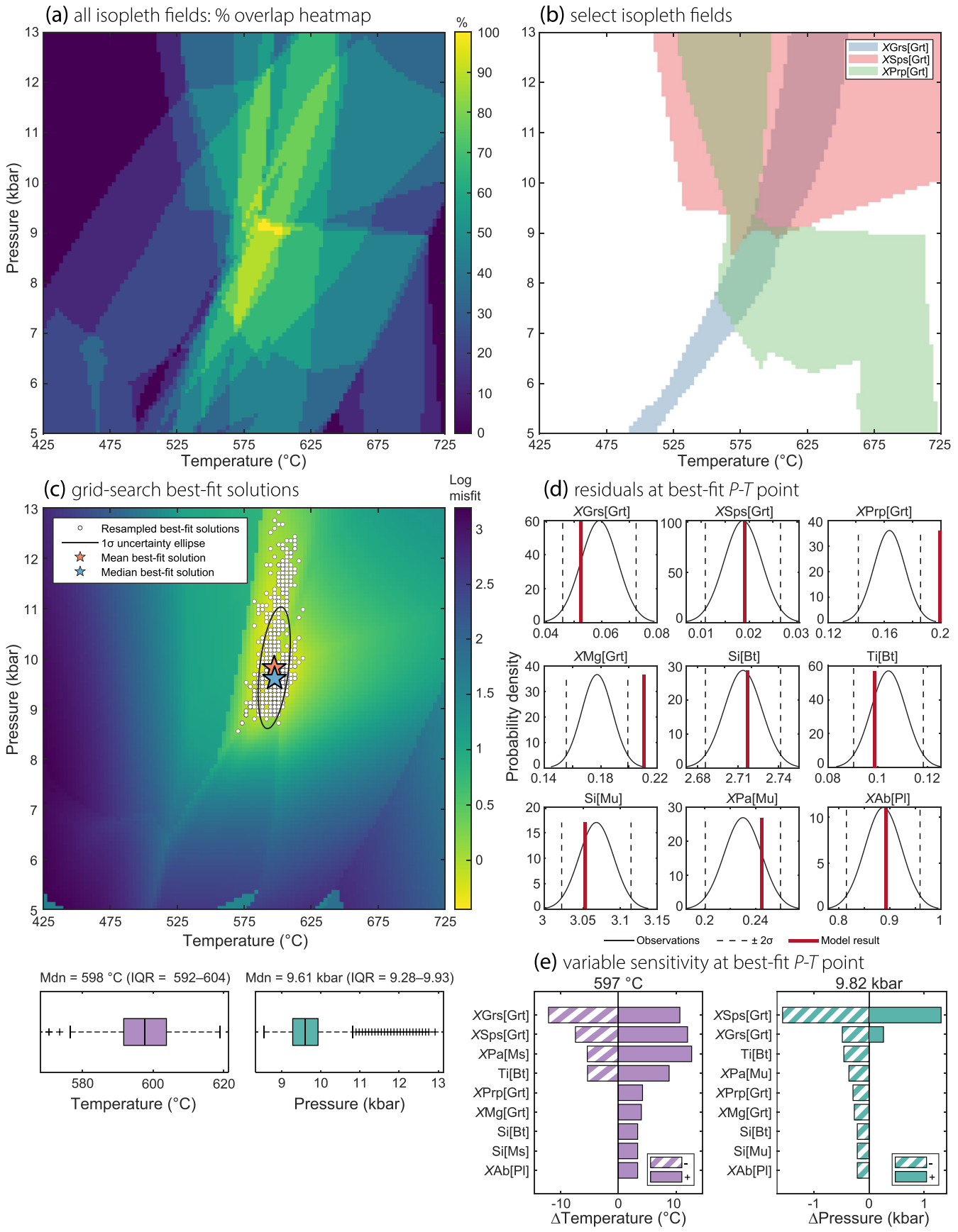

FIGURE 3 | Workflow example using natural sample ICSV13. (a) Overlapping isopleth 'fields' (2σ) of mineral measurements. (b) Intersection of X_{Grs}, X_{Prp} and X_{Sps} isopleth fields (2σ). (c) Grid-search best-fit solutions and heatmap (error surface) for bootstrapped mineral measurement data ($n = 1000$), with the mean and median best-fit result. (d) Data residuals at the median *P*–*T* point (598°C and 9.61 kbar), showing the fit between the model and the observations. (e) *T* and *P* tornado plots for sensitivity analysis of mineral composition variables at the mean *P*–*T* point (597°C and 9.82 kbar).

The method of bootstrap resampling should be chosen based on the data distribution or availability. Parametric bootstrapping, using a mean and standard deviation, is suitable for normally distributed data, whereas non-parametric bootstrapping, using the original data, is more appropriate for non-normal distributions. A minimum of 1000 resamples is recommended, though the required number can be evaluated by monitoring how the distribution of P and T solutions stabilizes with increasing resamples (Figure S1).

2.4.3 | Solution Assessment

Prior to inversion, the relationships among variables in P–T space should be interrogated to assess whether mutual equilibrium is likely for the selected variables for the range of values chosen for the modelling parameters (e.g., P–T range, $X_{Fe^{3+}}$, aH_2O). This can be visualized for all variables (e.g., Figure 3a) or for individual phases or variables (e.g., Figure 3b). A preliminary assessment can identify inconsistency between variables that may stem from clear geological or model uncertainty. However, in most cases, it is preferable to let the variables be removed through the diagnostics.

Fit diagnostics enable critical assessment of the reliability of inversion results (Table 2). If the total score of the quality of data fit (f_{total}) is above 1, variables with fit scores (f_i) exceeding 1 should be removed sequentially, starting with the most severe, until f_{total} falls below or is equal to 1. Further removal is generally unnecessary and not advised, as the L1-norm objective function is intrinsically robust to outliers (Claerbout and Muir 1973; Li et al. 2015; Ibraheem et al. 2021), and excessive pruning risks discarding meaningful information. In cases where no single outlier dominates but many variables contribute moderate misfit, the leave-one-out score ($f_{total(i)}$) may be used to identify the variable whose exclusion most effectively reduces f_{total} (lowest $f_{total(i)}$). The user may also examine the dispersion of the leave-one-out best-fit solutions to assess which variables, when removed, decrease dispersion and increase stability of the inversion. However, only variables that exhibit poor fit ($f_i > 1$) should be considered for removal in these cases. The above steps may then be followed. If widespread scatter persists despite these measures, it may reflect disequilibrium or retrogression (Powell and Holland 1994); and sequential removal is unlikely to resolve the issue. High sensitivity values (ΔP_i, ΔT_i) are not inherently problematic, but when they coincide with poor variable fit ($f_i > 1$), they may justify exclusion of the offending variables.

Once a satisfactory fit has been obtained, the best-fit solution and its uncertainty should ideally overlap the interpreted equilibrium assemblage field. Discrepancies may indicate inconsistencies between the analysed rock volumes, the scale of equilibrium or the definition of the equilibrium assemblage. Bootstrap resampling can reveal whether the uncertainty distribution is unimodal or multimodal. The distribution of the solution uncertainty can be assessed using histograms or the heatmap of solutions (Figure 3c). A multimodal distribution suggests that additional observations or external constraints (e.g., single-equilibrium thermobarometers) may be needed to discriminate among competing solutions. Significant local minima will increase the estimated uncertainty, reflected in a higher IQR. Final results should generally be reported using the median and IQR, which are suitable for non-normal distributions. Other recommendations for result reporting are included in the Supporting Information.

3 | Natural Examples

To illustrate the effectiveness of the workflow, we present results from analyses of a pelitic and a metabasic rock, demonstrating its performance across different model systems, solution models, and sets of variables. Specifically, we present a kyanite–staurolite schist (ICSV13) and a garnet amphibolite (ICSV117) from the Greater Himalayan Sequence in the Zanskar Himalaya, NW India. A characteristic photomicrograph of each sample is found in Figure S2, and detailed petrographic descriptions are included in the Supporting Information. Mineral compositions for each sample were inverted to determine best-fit P–T conditions and compared with classical thermobarometric methods. Details of the analytical setup, mineral recalculation procedure, formulation of bulk composition and forward modelling procedure are included in the Supporting Information. For each sample, the bulk rock composition, measured by X-ray fluorescence (XRF) under the assumption of chemical equilibrium at the rock scale, is included in Table 3 and the salient standard deviations and mean values for each mineral composition variable are provided in Table 4. The formatted workflow input files for each sample, including the mineral composition measurements and their corresponding forward modelled predictions, are included in Tables S1–S4.

3.1 | ICSV13

3.1.1 | Conventional Methods of Analysis

The inferred equilibrium assemblage at peak conditions for sample ICSV13 is kyanite–staurolite–garnet–biotite–muscovite–plagioclase–quartz–rutile–ilmenite–H_2O. Although the kyanite- and staurolite-present field directly represents the peak assemblage of all major phases, the narrow temperature range is at odds with the regular occurrence of this assemblage across numerous metamorphic terrains and wider temperature conditions (Pattison and Spear 2018). This discrepancy likely reflects either sluggish reaction kinetics that yield the metastable persistence of staurolite or the small free energy difference between staurolite and kyanite nucleation that enables kyanite to nucleate earlier, or staurolite later, than that predicted by the thermodynamic models (Pattison and Spear 2018; Cawood 2024). Therefore, the peak assemblage could also be assigned to either the staurolite-present or the kyanite-present field (Figure 4a).

TABLE 3 | Measured bulk composition via XRF of ICSV13 and ICSV117 in wt%.

Sample	SiO_2	Al_2O_3	Fe_2O_3	MnO	MgO	CaO	Na_2O	K_2O	TiO_2	P_2O_5	LOI	Total
ICSV13	61.23	19.13	7.10	0.09	2.65	0.47	1.52	4.12	0.98	0.09	1.96	99.31
ICSV117	47.80	14.42	14.92	0.19	6.39	9.99	2.41	0.75	2.12	0.18	0.34	99.51

TABLE 4 | Variables used for parametric bootstrap resampling in ICSV13 and ICSV117 (rounded to 3 decimal places).

Mineral	Grt				Bt			Ms		Pl	Amph			
Variable	X_{Grs}	X_{Sps}	X_{Prp}	X_{Mg}	Si	Ti	X_{Mg}	Si	X_{Cel}	X_{Pa}	X_{Ab}	Ti	Ts	Ed	Gln
ICSV13															
Mean	0.059	0.019	0.164	0.177	2.714	0.104	0.490	3.068	0.079	0.230	0.888				
σ	0.007	0.004	0.011	0.011	0.014	0.007	0.003	0.023	0.011	0.015	0.036				
ICSV117															
Mean	0.281		0.101	0.140	2.764	0.147	0.490				0.792	0.085	1.189	0.487	0.150
σ	0.013		0.009	0.009	0.005	0.009	0.015				0.012	0.012	0.034	0.028	0.010

In this case, the predominance of nearby assemblages being kyanite-bearing rather than staurolite- or kyanite+staurolite-bearing (Cawood et al. 2025), favours a kyanite-present field as the most likely choice for the peak assemblage field.

The peak assemblage field shows a wide *P–T* range over which the given rock composition may have equilibrated. Temperature ranges from ~600°C to in excess of the upper modelled temperature (725°C) and pressure is poorly constrained (~6 to > 13 kbar) owing to the dependence on the Ti-rich phases to define the phase boundaries, which are avoided here as a primary *P–T* constraint (e.g., Starr et al. 2020). Consequently, the broad range provided by the peak field in this sample is well suited to applying the workflow to further constrain the conditions of metamorphism. Using the Ti-in-biotite geothermometer calibration of Henry et al. (2005), the peak temperature is estimated at 594°C ± 24°C, and the pressure, using the av*P* function of THERMOCALC (Powell and Holland 1994) at the corresponding temperature, to a value of 9.3 ± 0.9 kbar (1σ). These results are both consistent with the peak assemblage field (Figure 4a).

3.1.2 | Grid-Search Inversion and Uncertainty Analysis

The workflow was performed on a 100 × 100 grid in *P–T* space from 425°C to 725°C and 5 to 13 kbar with 1000 random sets of samples drawn from the mineral composition data using bootstrap resampling assuming a normal distribution. Based on the interpreted peak mineral assemblage, 11 variables were used for this analysis: X_{Grs}, X_{Sps}, X_{Prp}, X_{Mg} of garnet; Si, Ti and X_{Mg} in biotite; Si content, X_{Pa}, and X_{Cel} of muscovite; and X_{Ab} of plagioclase (Table 4; see Table 1 for definitions). Staurolite and kyanite were not used as variables (the latter having no solution model) to avoid biasing the modelled stability fields of these phases. The *P–T* results are reported as median and IQR.

The mineral compositional variables produce a best-fit solution of 598°C (IQR 592°C–604°C) and 9.61 kbar (IQR 9.28–9.93 kbar; Figure 4c). This result and associated uncertainty show excellent agreement with the independent av*P* and Ti-in-biotite results (thermobarometer intersection) and overlap with the kyanite-present peak assemblage field (Figure 4b). During solution refinement, X_{Mg} in biotite and X_{Cel} were sequentially removed, the former due to poor fit ($f_{total} > 1$) and the latter due to poor fit coupled with strong influence on the solution (low $f_{total(i)}$). For the remaining nine variables, the residuals show the best-fit solution successfully fits seven within the 2σ range of the observed data (Figure 3d). X_{Prp} and X_{Mg} have poor fit, but the solution has low sensitivity to these variables. The best-fit solution is particularly sensitive to X_{Sps} and X_{Grs} with a ΔP_i of 1.58 and 0.49 kbar, respectively (Table 5). The high sensitivity to X_{Sps} is consistent with the close correlation of the end-member value with the proportion of garnet—a result of Mn mass balance in a system where garnet is the dominant Mn host (Spear 1993; Waters 2019).

The inversion shows that the natural data reproduce conditions most consistent with peak metamorphism in the modelled kyanite-present field, though the uncertainty distribution indicates that the staurolite-present or more temperature-restricted kyanite+staurolite field are also viable. Given the restricted *P–T* range defined by the overlap of the boundaries between

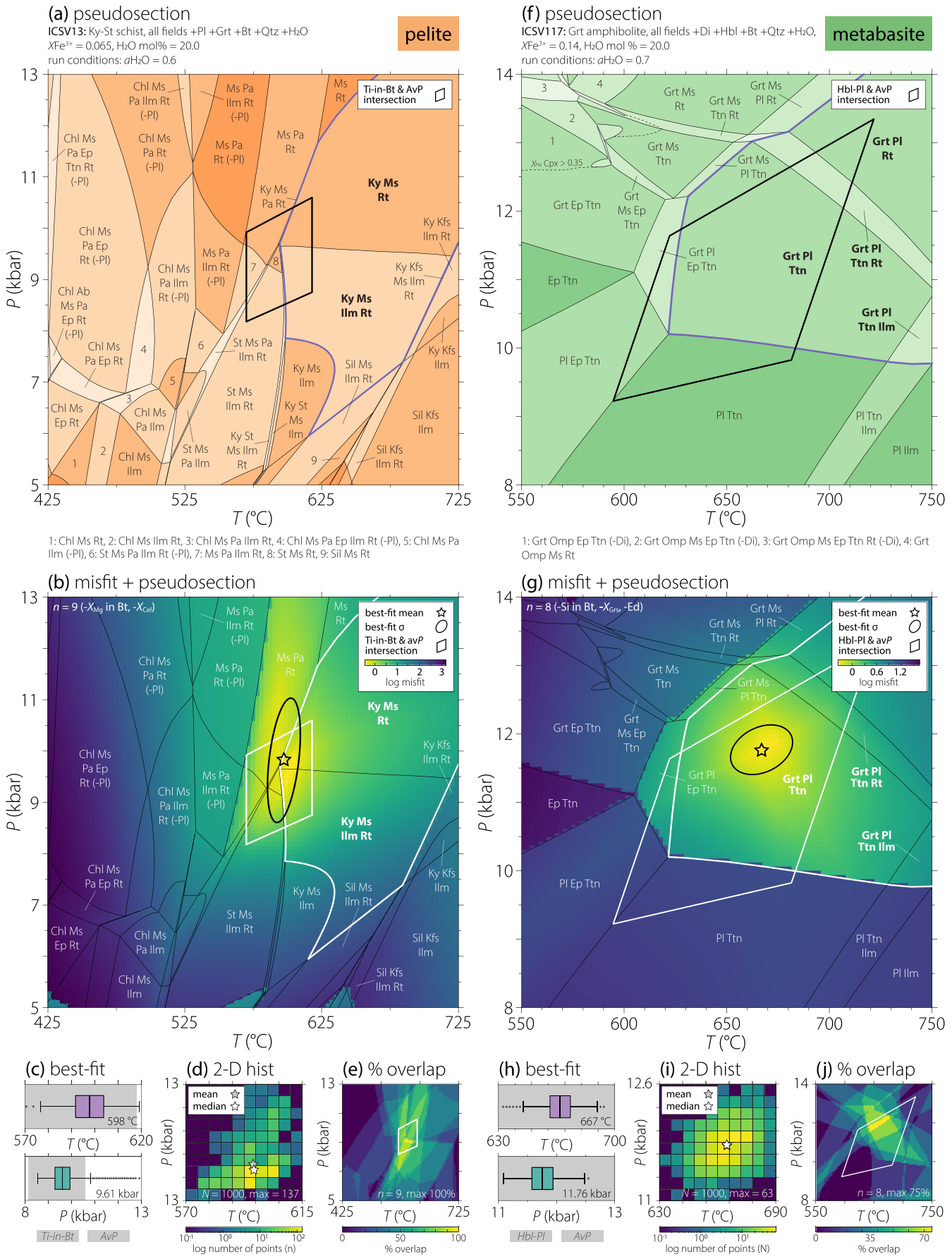

FIGURE 4 | Legend on next page.

FIGURE 4 | Example of compiled final result of ICSV13 (a–e) and ICSV117 (f–j). (a, f) Pseudosection with interpreted peak assemblage field outlined in purple. (b, g) Heatmap (error surface) of best-fit solutions showing the misfit of mineral composition variables, overlain with the corresponding pseudosection and the bootstrapped mean best-fit result and 1σ uncertainty. (c, h) Boxplots of bootstrapped *T* and *P* estimates with the grey bar indicating the range of the selected thermometer and av*P* results. (d, i) Log-scaled 2D-histogram bin plot of the bootstrapped data with the mean and median best-fit result marked by stars. (e, j) percent overlap of compositional isopleth fields at 2σ.

TABLE 5 | Result output and diagnostics for ICSV13. See definitions in Table 2.

Variable	f_i	$f_{total(i)}$	ΔT (°C)	ΔP (kbar)	$\mu_{obs} + 2\sigma$	$\mu_{obs} - 2\sigma$	Mod
X_{Grs}	0.4998	0.4836	12.03	0.4867	0.07243	0.04593	0.05256
X_{Sps}	0.05676	0.2883	11.9	1.579	0.02657	0.01084	0.01915
X_{Prp}	1.628	0.4	4.154	0.2916	0.1857	0.1415	0.1995
X_{Mg} Grt	1.519	0.4142	3.946	0.2674	0.1992	0.1556	0.2106
Si Bt	0.1276	0.5609	3.315	0.2133	2.741	2.686	2.717
Ti Bt	0.4031	0.5334	8.731	0.4593	0.1183	0.09032	0.09869
Si Ms	0.3182	0.5383	3.315	0.2133	3.115	3.021	3.053
X_{Pa}	0.5078	0.5887	12.61	0.3664	0.2597	0.2006	0.2451
X_{Ab}	0.07038	0.5626	3.315	0.2133	0.9596	0.8155	0.8926

Mean = 597°C ± 8°C, 9.82 ± 0.80 kbar (2σ).
Median = 598°C (IQR = 592°C–604°C), 9.61 kbar (IQR = 9.28–9.93 kbar).
f_{total} (median) = 0.57.
# of fitted variables = 7/9.
Model resolution = 3.03°C, 0.0808 kbar.
Vootstrap resamples = 1000.

fields and the uncertainty distribution, all solutions are broadly consistent with the microstructure and shared inclusion suite for both minerals, that imply coeval growth under similar conditions (Figure S2a; Cawood et al. 2025). More generally, the inversion framework demonstrates its value for precisely such cases, where ambiguities between multiple plausible assemblage fields can be tested and narrowed using the derived uncertainty distribution.

3.2 | ICSV117

3.2.1 | Conventional Methods of Analysis

The inferred equilibrium assemblage at peak conditions for sample ICSV117 is garnet–hornblende–biotite–plagioclase–quartz–ilmenite–titanite–H_2O. Petrographic observations show that titanite growth dominantly post-dates ilmenite growth, however it is unclear whether titanite represents peak conditions or growth during decompression from peak conditions. In either scenario, the relationship of Ti-bearing phases is not reproduced in a clockwise *P*–*T* path on the modelled diagram; therefore, as applied for ICSV13, the stability fields of the Ti-rich phases are not prioritized. Furthermore, the modelled presence or absence of clinopyroxene is not deemed relevant to phase boundaries in clinopyroxene-absent assemblages owing to its predicted overstability in modelled metabasic systems (Forshaw et al. 2019). Therefore, the upper-pressure boundary of the peak assemblage field is delimited by the presence of muscovite at higher pressures and the absence of garnet at lower pressures. The peak assemblage field extends for a greater range of temperatures than modelled (620°C–750°C) and from ~10 kbar to higher pressures than modelled (> 14 kbar; Figure 4f). Using the hornblende-plagioclase exchange geothermometer calibration of Holland and Blundy (1994), the peak temperature is constrained to 644°C ± 40°C, and the pressure, using the av*P* function of THERMOCALC at the matching temperature, to a value of 10.8 ± 1.2 kbar (1σ). These results show excellent agreement with the peak assemblage field (Figure 4f).

3.2.2 | Grid-Search Inversion and Uncertainty Analysis

The inversion workflow was performed on a 100 × 100 grid in *P*–*T* space from 550°C to 750°C and 8 to 14 kbar with 1000 random sets of samples drawn from the mineral composition data using bootstrap resampling assuming a normal distribution. Based on the interpreted peak mineral assemblage, 11 variables were used for this analysis: X_{Grs}, X_{Prp}, X_{Mg} of garnet; Ti, Si and X_{Mg} in biotite; X_{Ab} of plagioclase; Ti content, and Ts (tschermakite, Al(T)-Na(A)-K(A)), Ed (edenite, Na(A) + K(A)), and Gln (glaucophane, Na(M4)) vectors of amphibole (Table 4; see Table 1 for variable definitions). Amphibole vectors were used to reduce dependency of the result on overestimated (Al and A-site Na) or underestimated (Si, Ca and A-site K) cations (Forshaw et al. 2019).

The mineral compositional variables produce a median best-fit solution at 667°C (IQR = 661°C–673°C) and 11.76 kbar

TABLE 6 | Result output and diagnostics for ICSV117. See definitions in Table 2.

Variable	f_i	$f_{total(i)}$	ΔT (°C)	ΔP (kbar)	$\mu_{obs} + 2\sigma$	$\mu_{obs} - 2\sigma$	Mod
X_{Prp}	0.2188	0.7681	10.46	0.1434	0.1188	0.08252	0.09671
X_{Mg} Grt	0.4122	0.7718	5.495	0.09814	0.1577	0.1223	0.1473
Ti Bt	0.02354	0.833	13.77	0.2064	0.1650	0.1298	0.1478
X_{Mg} Bt	0.2958	0.776	5.929	0.1048	0.5210	0.4596	0.4994
X_{Ab}	1.502	0.61	2.214	0.04892	0.8162	0.7686	0.7567
Ti Amph	1.504	0.6097	3.617	0.06997	0.1097	0.05974	0.04716
Gln	0.06948	0.8758	5.442	0.4722	0.1697	0.1311	0.1491
Ts	1.746	0.575	2.214	0.04892	1.257	1.121	1.308

Mean = 667°C ± 10°C, 11.77 ± 0.24 kbar (2σ).
Median = 667°C (IQR = 661°C–673°C), 11.76 kbar (IQR = 11.64–11.94 kbar).
f_{total} (median) = 0.721.
# of fitted variables = 5/8.
Model resolution = 2.02°C, 0.0606 kbar.
Bootstrap resamples = 1000.

(IQR = 11.64–11.94 kbar; Figure 4g,h; Table 6), in agreement with the thermobarometer intersection and peak assemblage field. Si in biotite, X_{Grs}, and the Ed vector were sequentially removed due to poor fit ($f_i > 1$; Table 6). For the final eight variables, the residuals show the best-fit solution successfully fits five within the 2σ range of the observed data (Figure S3a). X_{Ab} and Ti in amphibole and the Ts vector show poor fit, but the inversion has low sensitivity to these variables (Table 6 and Figure S3b). The best-fit temperature is most sensitive to X_{Prp} and Ti in Bt (ΔT_i of 10°C and 14°C, respectively) and pressure is sensitive to the Gln vector and Ti in biotite, with ΔP_i values of 0.47 and 0.21 kbar, respectively (Figure S3b). Although the Ti-in-biotite variable is relatively pressure insensitive, the value determines the intersection point with variables which are more pressure sensitive (i.e., sloping *P–T* gradients) and therefore has an important role to play in determining the pressure of the solution (Figure 4j).

Initial thermobarometric analyses were performed for ICSV117 assuming a garnet-absent assemblage, based on the lack of garnet observed at outcrop, hand-sample and thin-section scales. Given the sample's location within a garnet-bearing metamorphic zone of the metabasic sequence (Cawood et al. 2025), this absence was attributed to subtle bulk compositional variation, as observed in other samples from the region. However, the inversion consistently returned best-fit solutions within the garnet-bearing stability field across varied parameter ranges, contradicting the a priori assemblage. Subsequent targeted reconnaissance identified accessory garnet grains ranging from 140 to 180 μm, validating that the inversion result was resilient despite the initial misclassification of the equilibrium assemblage. This outcome aligns with prior findings that have demonstrated good agreement between predicted and observed garnet modes in metabasic systems (Forshaw et al. 2019). As previously outlined, the space in which the misfit function identifies a best-fit solution is inherently governed by the modelled stability ranges of the phases of the chosen variables. Consequently, phases that are either not present in the observed assemblage or not included in the inversion do not necessarily impact the solution. This underscores the need to critically evaluate how the best-fit result relates to the interpreted equilibrium assemblage field. We note that such resilience is case specific and in this situation was contingent on the acquisition of whole-rock XRF analyses for the bulk rock composition; erroneous assemblage assumptions could have more serious consequences where effective or reactive bulk compositions are used.

4 | Discussion

4.1 | Comparison to Other Quantitative Workflows

Using petrological data to quantitatively invert for pressure and temperature is well established. The av*PT* function of THERMOCALC (Powell and Holland 1994) uses the activities of end-members involved in balanced independent chemical equilibria from an internally consistent thermodynamic dataset to calculate the *P–T* conditions. An iterative, least-squares inversion is used to find the optimal *P–T* condition that maximizes the consistency between each independent chemical equilibrium involved within the inversion (Powell and Holland 1994). The same approach applies for av*P* and av*T* calculations, although these are calculated directly without iteration (Powell and Holland 1988). This approach calculates uncertainties stemming from the model, in contrast to observational uncertainties derived from the mineral measurements considered in this method. TWEEQU (Thermobarometry With Estimation of EQUilibration state) follows a similar multi-equilibrium approach, calculating all possible equilibria for the selected phase components from an internally consistent thermodynamic database, with uncertainties estimated from the weighted scatter of equilibria intersections (Berman 1991). The subsequent winTWQ refined this by emphasizing a more robust independent set of equilibria (Berman 2007). Although these methods are powerful and have been widely used, they remain independent from phase equilibrium modelling.

Bingo-Antidote uses the forward models calculated by Theriak-Domino to perform a global optimization of *P* and *T* (Duesterhoeft and Lanari 2020) for the observed phase assemblage, mineral modal proportions and mineral compositions.

Bingo-Antidote is particularly powerful due to its integration with XMapTools (Lanari et al. 2019) and thus its ability to link directly to compositional phase maps and examine the impact of local bulk composition variation on resulting *P–T* estimates. IntersecT (Nerone et al. 2025) builds on a similar principle using outputs from Perple_X to provide a quantitative framework for evaluating the quality of fit between model-predicted isopleths and measured mineral compositions. Some key differences between these workflows and the method proposed here are discussed in the Supporting Information. Most notably, uncertainty is estimated quite differently. In Bingo-Antidote, measurement uncertainties are incorporated into its definition of the objective function. Lower values of their objective function (quality factor, Q_{total}) indicate that the inversion is closer to the mean observed value for any given data variable. Uncertainty is calculated as the region of *P–T* space yielding Q_{total} scores within 2% of the optimum. This can be thought of the goodness-of-fit error, which quantifies how well different potential solutions describe the mean value for each variable. IntersecT combines the quality factor metric of Bingo-Antidote for compositional variables (Q_{cmp}) with a reduced χ^2 statistic, which explicitly weights each phase according to how well its measured composition is reproduced within its observed uncertainty. In contrast, LinaForma does not define uncertainty from a single optimum solution. Instead, it estimates uncertainties through bootstrap resampling of mineral measurements, generating multiple realizations to produce a distribution of possible *P–T* solutions. This method emphasizes how uncertainties in the underlying data translate into variability in the inferred conditions.

4.2 | Advantages and Limitations of the New Workflow

4.2.1 | Grid-Search Inversion

The grid-search inversion offers a systematic approach to identify the global minimum of the misfit function and determine the best-fit solution within the selected model space. By discretizing *P–T* space into a grid of forward models and calculating the misfit at each grid point (Figure 2a), this method ensures the global minimum is located, provided the grid range and precision are appropriate. The grid search is also advantageous because it is adaptable to various combinations of model parameters, such as *T–X* and *P–X*, making it applicable across a broad range of petrological modelling scenarios. Furthermore, the workflow is equally applicable to higher-dimensional analyses (e.g., *P–T–X*). However, the grid-search approach introduces computational challenges as the number of trial solutions increases exponentially with increasing dimensionality. Recent advances in forward modelling software (e.g., Riel et al. 2022) have significantly reduced the computational time required for these calculations, allowing the extension of this workflow to higher dimensions and reducing the need for assigning parameters a priori (e.g., $X_{Fe^{3+}}$, aH_2O).

4.2.2 | Misfit/Objective Function

The workflow employs the L1-norm misfit function, a robust measure of fit that is widely used across scientific disciplines because of its resilience to outliers, outperforming L2-norm (least-squares) or chi-squared functions in this regard (Claerbout and Muir 1973; Li et al. 2015; Ibraheem et al. 2021). This makes the method particularly well suited for petrological systems where significant outliers are common. In addition, the leave-one-out calculation allows the user to diagnose variables that disproportionately affect the inversion and ensure that high-leverage and poorly fitting variables do not bias the final solution.

The inversion does not directly resolve or use the stable phase assemblage unless the variables are specifically defined to do so and can therefore also be applied with caution in metastable systems. The misfit function seeks solutions in which all phases included in the selected variables are of the correct composition and/or modal proportion, thereby defined by where these phases are predicted to be stable. Therefore, the boundaries of the result are inherently dependent on the variables employed in the inversion. The lack of strict relationship between the misfit function and a user-defined equilibrium assemblage field has several benefits: (1) The assemblage field corresponding to a mineral assemblage in a pseudosection may be smaller than the estimated uncertainty (Powell and Holland 2008; Waters 2019); (2) field boundaries defined by small modal proportion or accessory phases may not be reliable (Weller et al. 2024); and (3) assemblage field boundaries, mineral modal proportion contours, and mineral compositional isopleths show relatively decreasing uncertainties and increasing precision (Waters 2019). However, where mismatch occurs between an inversion result and the inferred equilibrium assemblage field, this should in all cases be critically assessed.

The misfit function does not inherently penalize inversions using a small number of variables. However, the number of variables will have a significant impact on the *P–T* uncertainty derived from bootstrap resampling, discussed below. This workflow deliberately avoids variable weighting, such that all variables are treated as equally valid in the inversion. This approach is advantageous in scenarios where the relative importance of variables is difficult to determine or where weighting would introduce significant bias into the results. A limitation of this approach is that highly influential variables can disproportionately affect the solution; however, this is mitigated by quantifying variable leverage with the influence analysis.

4.2.3 | Uncertainty Analysis

Monte Carlo methods, such as bootstrap resampling, are particularly well suited to estimating uncertainty in non-linear problems such as *P–T* inversion, where the combined effects of random and systematic errors cannot be calculated directly (Menke 1984). The application of bootstrap resampling to the observed data allows users to empirically estimate the variability, or uncertainty, of the inverse solution (Figure 2b). It may also be used to identify any significant local minima that may provide alternative hypotheses and to evaluate the sensitivity of the final result to the different input variables (Figure 3e).

Although the workflow incorporates multiple sources of uncertainty stemming from the observations, not all uncertainties are fully addressed. Uncertainty in the parameters used during modelling and the underlying thermodynamic end-member datasets and a–X relations are not directly examined by bootstrap resampling. Nevertheless, the method inherently incorporates some of these uncertainties due to reliance on Monte Carlo–style methods. With the reduced computational times of forward modelling (e.g., Riel et al. 2022), it is now possible to include Monte Carlo simulations of the forward model itself, systematically varying input parameters, solution models and end-member properties to evaluate the influence of model uncertainty on the resulting P–T solutions.

5 | Conclusions

Accurately quantifying the petrological parameters of metamorphic rocks is crucial for understanding a broad range of processes in both the solid and surficial Earth, including identifying geothermal gradients in the subsurface and sources of economically valuable raw materials (e.g., critical metals), understanding climate and Earth system feedbacks, reconstructing the tectonometamorphic evolution of terrains, and informing broader geodynamic models. The ability to understand and quantify uncertainties in derived model parameters, such as P–T conditions, is essential to ensuring that results can be interpreted within a defined confidence range. This is particularly important in scenarios where geological or petrological interpretations hinge on relatively small variations in pressure and/or temperature (e.g., Pattison and DeBuhr 2015). Although many sources of uncertainty in phase equilibrium modelling cannot be estimated or are difficult to quantify, for those that can be, there should be an attempt to do so (Powell and Holland 2008). The key conclusions of this study are:

1. The new workflow, LinaForma, provides a quantitative framework for calculating the best-fit P–T conditions (or other petrological parameters) and associated uncertainties for a given rock system. The technique identifies the best-fit solution by comparing observed data, such as mineral compositions and/or modal proportions, with forward modelled predictions across a user-defined P–T grid. Bootstrap resampling (repeated sampling with replacement) quantifies the uncertainty of the inverse solution and assesses its sensitivity to input variable uncertainty. Three diagnostic metrics—quality of data fit, variable influence and variable sensitivity—are incorporated to validate and refine the results.
2. Application to natural samples demonstrates that peak P–T conditions and uncertainty estimates for both pelitic and metabasic compositions align with classical thermobarometric methods. Local discrepancies help assess model limitations and refine prior interpretations, such as the equilibrium assemblage.
3. The workflow is compatible with any forward modelling software, supports flexible variable selection, performs a systematic grid-search inversion in multidimensional parameter space and uses a robust L1-norm misfit function that is relatively resistant to outliers while also providing uncertainty and sensitivity analysis through bootstrap resampling. Its main limitations are the high computational cost of exploring grids in more than two or three dimensions and the lack of explicit quantification of uncertainties inherited from the underlying thermodynamic end-member dataset and solution models.

Acknowledgements

T.M.-C. would like to thank BHP and an Oxford-Radcliffe Graduate Scholarship for supporting his PhD research. I.P.C. acknowledges support from the Natural Environment Research Council (NERC; grant NE/L002612/1) and the Hong Kong RGC Co-funding Mechanism on Joint Laboratories with the Chinese Academy of Sciences (grants JLFS/P-702/24 and 17308023). We are grateful to Eleanor Green, Geoff Clarke, an anonymous reviewer, and handling editor Katy Evans for comments that substantially improved the workflow and clarity of the manuscript. We also thank Pierre Lanari for informal feedback, Sara Nerone for discussions on variable selection, and Richard Palin and Dave Waters for guidance throughout this work.

Conflicts of Interest

The authors declare no conflicts of interest.

Data Availability Statement

The outlined workflow, LinaForma, is available via the GitHub repository https://github.com/QuantPT/LinaForma.

References

Berman, R. G. 1988. "Internally-Consistent Thermodynamic Data for Minerals in the System Na_2O-K_2O-CaO-MgO-FeO-Fe_2O_3-Al_2O_3-SiO_2-TiO_2-H_2O-CO_2." *Journal of Petrology* 29, no. 2: 445–522. https://doi.org/10.1093/petrology/29.2.445.

Berman, R. G. 1991. "Thermobarometry Using Multi-Equilibrium Calculations; a New Technique, With Petrological Applications." *Canadian Mineralogist* 29: 833–855.

Berman, R. G. 2007. "winTWQ (Version 2.3): A Software Package for Performing Internally-Consistent Thermobarometric Calculations." Geological Survey of Canada, Open File, 5462.

Cawood, I. P. 2024. "Structural and Metamorphic Evolution of the Zanskar Himalaya, Suru Valley Region, NW India." PhD thesis, University of Oxford.

Cawood, I. P., M. R. St-Onge, O. M. Weller, M. P. Searle, D. J. Waters, and T. Ahmad. 2025. "Structural and Metamorphic Architecture of the Zanskar Himalaya, Suru Valley Region, NW India: Implications for the Evolution of the Himalayan Metamorphic Core." *GSA Bulletin* 137, no. 1-2: 1–28. https://doi.org/10.1130/B37241.1.

Claerbout, J. F., and F. Muir. 1973. "Robust Modeling With Erratic Data." *Geophysics* 38, no. 5: 826–844. https://doi.org/10.1190/1.1440378.

Connolly, J. 1990. "Multivariable Phase Diagrams: An Algorithm Based on Generalized Thermodynamics." *American Journal of Science* 290: 666–718. https://doi.org/10.2475/ajs.290.6.666.

Connolly, J. 2005. "Computation of Phase Equilibria by Linear Programming: A Tool for Geodynamic Modeling and Its Application to Subduction Zone Decarbonation." *Earth and Planetary Science Letters* 236, no. 1–2: 524–541. https://doi.org/10.1016/j.epsl.2005.04.033.

de Capitani, C., and T. H. Brown. 1987. "The Computation of Chemical Equilibrium in Complex Systems Containing Non-Ideal Solutions." *Geochimica et Cosmochimica Acta* 51, no. 10: 2639–2652. https://doi.org/10.1016/0016-7037(87)90145-1.

de Capitani, C., and K. Petrakakis. 2010. "The Computation of Equilibrium Assemblage Diagrams With Theriak/Domino Software." *American Mineralogist* 95, no. 7: 1006–1016. https://doi.org/10.2138/am.2010.3354.

Duesterhoeft, E., and P. Lanari. 2020. "Iterative Thermodynamic Modelling—Part 1: A Theoretical Scoring Technique and a Computer Program (Bingo-Antidote)." *Journal of Metamorphic Geology* 38, no. 5: 527–551. https://doi.org/10.1111/jmg.12538.

Efron, B. 1979. "Bootstrap Methods: Another Look at the Jackknife." *Annals of Statistics* 7, no. 1: 1–26. https://doi.org/10.1007/978-1-4612-4380-9_41.

Forshaw, J. B., D. J. Waters, D. R. M. Pattison, R. M. Palin, and P. Gopon. 2019. "A Comparison of Observed and Thermodynamically Predicted Phase Equilibria and Mineral Compositions in Mafic Granulites." *Journal of Metamorphic Geology* 37, no. 2: 153–179. https://doi.org/10.1111/jmg.12454.

Gordon, T. M. 1992. "Generalized Thermobarometry: Solution of the Inverse Chemical Equilibrium Problem Using Data for Individual Species." *Geochimica et Cosmochimica Acta* 56, no. 5: 1793–1800. https://doi.org/10.1016/0016-7037(92)90310-F.

Henry, D. J., C. V. Guidotti, and J. A. Thomson. 2005. "The Ti-Saturation Surface for Low-to-Medium Pressure Metapelitic Biotites: Implications for Geothermometry and Ti-Substitution Mechanisms." *American Mineralogist* 90: 316–328. https://doi.org/10.2138/am.2005.1498.

Holland, T., and J. Blundy. 1994. "Non-Ideal Interactions in Calcic Amphiboles and Their Bearing on Amphibole-Plagioclase Thermometry." *Contributions to Mineralogy and Petrology* 116, no. 4: 433–447. https://doi.org/10.1007/BF00310910.

Holland, T. J. B., and R. Powell. 1998. "An Internally Consistent Thermodynamic Data Set for Phases of Petrological Interest." *Journal of Metamorphic Geology* 16, no. 3: 309–343. https://doi.org/10.1111/j.1525-1314.1998.00140.x.

Hoschek, G. 2004. "Comparison of Calculated P-T Pseudosections for a Kyanite Eclogite From the Tauern Window, Eastern Alps, Austria." *European Journal of Mineralogy* 16, no. 1: 59–72. https://doi.org/10.1127/0935-1221/2004/0016-0059.

Ibraheem, I. M., B. Tezkan, and R. Bergers. 2021. "Integrated Interpretation of Magnetic and ERT Data to Characterize a Landfill in the North-West of Cologne, Germany." *Pure and Applied Geophysics* 178, no. 6: 2127–2148. https://doi.org/10.1007/s00024-021-02750-x.

Lanari, P., S. Ferrero, P. Goncalves, and E. G. Grosch. 2019. "Metamorphic Geology: Progress and Perspectives." *Geological Society, London, Special Publications* 478, no. 1: 1–12. https://doi.org/10.1144/SP478-2018-186.

Li, C.-N., Y.-H. Shao, and N.-Y. Deng. 2015. "Robust L1-Norm Two-Dimensional Linear Discriminant Analysis." *Neural Networks* 65: 92–104. https://doi.org/10.1016/j.neunet.2015.01.003.

Menke, W. 1984. *Geophysical Data Analysis: Discrete Inverse Theory*. Academic Press.

Nerone, S., P. Lanari, H. Dominguez, J. B. Forshaw, C. Groppo, and F. Rolfo. 2025. "IntersecT: A Python Script for Quantitative Isopleth Thermobarometry of Equilibrium and Disequilibrium Systems." *Computers & Geosciences* 202, no. 105: 949. https://doi.org/10.1016/j.cageo.2025.105949.

Palin, R. M., O. M. Weller, D. J. Waters, and B. Dyck. 2016. "Quantifying Geological Uncertainty in Metamorphic Phase Equilibria Modelling; a Monte Carlo Assessment and Implications for Tectonic Interpretations." *Geoscience Frontiers* 7, no. 4: 591–607. https://doi.org/10.1016/j.gsf.2015.08.005.

Pattison, D. R. M., and C. L. DeBuhr. 2015. "Petrology of Metapelites in the Bugaboo Aureole, British Columbia, Canada." *Journal of Metamorphic Geology* 33, no. 5: 437–462. https://doi.org/10.1111/jmg.12128.

Pattison, D. R. M., and F. S. Spear. 2018. "Kinetic Control of Staurolite–Al_2SiO_5 Mineral Assemblages: Implications for Barrovian and Buchan Metamorphism." *Journal of Metamorphic Geology* 36, no. 6: 667–690. https://doi.org/10.1111/jmg.12302.

Powell, R., and T. Holland. 1988. "An Internally Consistent Dataset With Uncertainties and Correlations: 3. Applications to Geobarometry, Worked Examples and a Computer Program." *Journal of Metamorphic Geology* 6, no. 2: 173–204. https://doi.org/10.1111/j.1525-1314.1988.tb00415.x.

Powell, R., and T. Holland. 1994. "Optimal Geothermometry and Geobarometry." *American Mineralogist* 79: 120–133.

Powell, R., and T. J. B. Holland. 2008. "On Thermobarometry." *Journal of Metamorphic Geology* 26, no. 2: 155–179. https://doi.org/10.1111/j.1525-1314.2007.00756.x.

Riel, N., B. J. P. Kaus, E. C. R. Green, and N. Berlie. 2022. "MAGEMin, an Efficient Gibbs Energy Minimizer: Application to Igneous Systems." *Geochemistry, Geophysics, Geosystems* 23, no. 7: e2022GC010,427. https://doi.org/10.1029/2022GC010427.

Spear, F. S. 1993. *Metamorphic Phase Equilibria and Pressure-Temperature-Time-Paths*. Mineralogical Society of America.

Spear, F. S., D. R. Pattison, and J. T. Cheney. 2016. "The Metamorphosis of Metamorphic Petrology." In *The Web of Geological Sciences: Advances, Impacts, and Interactions II*, edited by M. Bickford. Geological Society of America. https://doi.org/10.1130/2016.2523(02).

Starr, P. G., D. R. M. Pattison, and D. E. Ames. 2020. "Mineral Assemblages and Phase Equilibria of Metabasites From the Prehnite–Pumpellyite to Amphibolite Facies, With the Flin Flon Greenstone Belt (Manitoba) as a Type Example." *Journal of Metamorphic Geology* 38, no. 1: 71–102. https://doi.org/10.1111/jmg.12513.

Štípská, P., and R. Powell. 2005. "Constraining the P–T Path of a MORB-Type Eclogite Using Pseudosections, Garnet Zoning and Garnet-Clinopyroxene Thermometry: An Example From the Bohemian Massif." *Journal of Metamorphic Geology* 23, no. 8: 725–743. https://doi.org/10.1111/j.1525-1314.2005.00607.x.

Vance, D., and E. Mahar. 1998. "Pressure-Temperature Paths From P-T Pseudosections and Zoned Garnets: Potential, Limitations and Examples From the Zanskar Himalaya, NW India." *Contributions to Mineralogy and Petrology* 132: 225–245.

Waters, D. J. 2019. "Metamorphic Constraints on the Tectonic Evolution of the High Himalaya in Nepal: The Art of the Possible." *Geological Society, London, Special Publications* 483: 325–375. https://doi.org/10.1144/sp483-2018-187.

Weller, O. M., T. J. B. Holland, C. R. Soderman, et al. 2024. "New Thermodynamic Models for Anhydrous Alkaline-Silicate Magmatic Systems." *Journal of Petrology* 65, no. 10: egae098. https://doi.org/10.1093/petrology/egae098.

Supporting Information

Additional supporting information can be found online in the Supporting Information section. **Data S1:** Supporting Information. **Table S1:** ICSV13 mineral composition measurements for LinaForma. **Table S2:** ICSV13 forward model for LinaForma. **Table S3:** ICSV117 mineral composition measurements for LinaForma. **Table S4:** ICSV117 forward model for LinaForma.